Journal of Geophysical Research: Atmospheres

RESEARCH ARTICLE
10.1002/2017JD028007

Changes in Stratospheric Transport and Mixing During Sudden Stratospheric Warmings

A. de la Cámara[1,2,3], **M. Abalos**[2], **and P. Hitchcock**[1,4]

[1]National Center for Atmospheric Research, Boulder, CO, USA, [2]Departamento Física de la Tierra y Astrofísica, Universidad Complutense de Madrid, Madrid, Spain, [3]Instituto de Geociencias (CSIC-UCM), Madrid, Spain, [4]Laboratoire de Météorologie Dynamique/IPSL, École Polytechnique, Université Paris-Saclay, Palaiseau, France

Key Points:

- After the onset of SSWs, the residual circulation decelerates and mixing is enhanced, persisting for 2 months in the lower stratosphere
- Sufficiently deep SSWs have a stronger and more persistent response in the meridional circulation and isentropic mixing
- Diffusive potential vorticity fluxes remain high in the lower stratosphere, a feature not seen in more conventional zonal-mean eddy fluxes

Correspondence to:
A. de la Cámara,
acamarai@ucm.es

Citation:
de la Cámara, A., Abalos, M., & Hitchcock, P. (2018). Changes in stratospheric transport and mixing during sudden stratospheric warmings. *Journal of Geophysical Research: Atmospheres*, *123*, 3356–3373. https://doi.org/10.1002/2017JD028007

Received 3 NOV 2017
Accepted 1 MAR 2018
Accepted article online 6 MAR 2018
Published online 6 APR 2018

Abstract The extreme disruptions of the wintertime stratospheric circulation during sudden stratospheric warmings (SSW) have large effects on tracer concentrations through alterations in transport. This study analyzes the changes in residual circulation and isentropic mixing associated with SSWs, by performing composites using reanalysis (European Centre for Medium-Range Weather Forecasts Re-Analysis Interim) and simulations of the Whole Atmosphere Community Climate Model. The advective Brewer-Dobson circulation accelerates around 15 days prior to the wind reversal at 60°N, 10 hPa during the onset of SSWs. Soon afterward, it decelerates, leading to reduced advective transport into the vortex and descent over the pole, which persist for more than 2 months below 30 hPa. The isentropic mixing has a distinct signature in altitude: It is enhanced at the central date of the SSW in the midstratosphere (about 10 hPa or 800 K), and this signal is delayed and more persistent at lower altitudes. It is shown that sufficiently deep SSWs (particularly those related to Polar-night Jet Oscillation events) have a stronger response in the Brewer-Dobson circulation and mixing. In particular, both the polar downwelling and the tropical upwelling are anomalously weak in the lower stratosphere for 90 days after the onset of Polar-night Jet Oscillation events. The redistribution of potential vorticity during the life cycle of SSWs is discussed due to its relevance for the stratospheric circulation. It is shown that the diffusive flux of potential vorticity, calculated in equivalent latitude coordinates, remains anomalously high in the lower stratosphere, a feature that is not seen in more conventional advective eddy fluxes across latitude circles.

1. Introduction

Sudden stratospheric warmings (SSWs) are extreme dynamical phenomena that have global impacts on the middle atmosphere circulation. In a matter of few days the polar vortex is severely disrupted, the zonal-mean wind reverses direction throughout most of the polar stratosphere, and polar temperatures increase several tens of degrees (e.g., Butler et al., 2015; Charlton & Polvani, 2007). The enhanced wave forcing in the polar stratosphere that drives these events accelerates the Brewer-Dobson circulation (BDC), connecting the polar and tropical circulations (e.g., Haynes et al., 1991). Also, the polar stratospheric conditions after SSWs prevent the propagation of planetary waves (Charlton & Polvani, 2007; Limpasuvan et al., 2004), which are directed toward the subtropics and tropics where they induce circulation changes (Gómez-Escolar et al., 2014). Using reanalysis data, Gómez-Escolar et al. (2014) isolated the tropical temperature signal of the SSWs from the quasi-biennial oscillation signal (e.g., Baldwin et al., 2001; Ebdon, 1960) and showed that the tropical cooling during SSW events (Barnett et al., 1975; Fritz & Soules, 1970, 1972) is mainly due to enhanced tropical upwelling in agreement with early SSW modeling studies (e.g., Dunkerton et al., 1981).

The disruption of the polar stratospheric circulation during SSWs also induces big changes in tracer constituents, whose zonal-mean concentrations are primarily determined by a balance between the meridional advection by the BDC, rapid isentropic stirring and mixing that follows planetary wave breaking, and chemical production and loss (e.g., Plumb, 2002). Taking advantage of global coverage of tracer distribution data derived from satellite instruments, several studies for individual winters in the 2000s have shown that the breakdown of the transport barrier at the vortex edge led to rapid, widespread mixing of trace gases such as CO, H_2O, CH_4, and N_2O (e.g., Manney & Lawrence, 2016; Manney et al., 2008, 2009; Manney, Lawrence, Santee, Livesey, et al., 2015; Manney, Lawrence, Santee, Read, et al., 2015). This series of papers also highlighted the intraevent variability in the response of the tracers, particularly when the activation of chemical reactions depends on meeting certain thresholds. Using the Chemical Lagrangian Model of the Stratosphere to study the SSW of January 2009, Tao et al. (2015) concluded that mixing across the weakened vortex edge accounted for a large fraction of the ozone changes in the polar stratosphere after the onset of the SSW.

The present study aims at providing the first overall picture, in a composite sense, of the changes in stratospheric transport and mixing induced during SSW events, highlighting in particular their relevance for the potential vorticity (PV) budget. We analyze the anomalies of both the advective BDC and the isentropic mixing in reanalysis output and 240 years of climate simulations with the Whole Atmosphere Community Climate Model (WACCM). We use calculations of the effective diffusivity (Nakamura, 1996) to extract the mixing characteristics of the flow. This diagnostic is a useful tool for identifying transport barriers and mixing regions (Haynes & Shuckburgh, 2000a, 2000b; Nakamura & Ma, 1997), such as those at the vortex edge and the surf zone, respectively. Abalos, Legras, et al. (2016) have recently analyzed the interannual variability of mixing in European Centre for Medium-Range Weather Forecasts Re-Analysis Interim (ERAI) using the effective diffusivity and shown that the variability associated with the annular modes dominates the interannual variations of stratospheric mixing in the polar vortices, although no connection was found with the surf zone. We pay special attention to SSWs whose wind and temperature signals reach well into the lower stratosphere, associated with the so called Polar-night Jet Oscillation (PJO) events (Kodera et al., 2000; Kuroda & Kodera, 2001). Several studies have shown that the circulation anomalies during such “PJO events” are stronger and last longer (up to 3 months) throughout the stratospheric column (Hitchcock & Shepherd, 2013; Hitchcock, Shepherd, & Manney, 2013; Hitchcock, Shepherd, Taguchi, et al., 2013). Our results show that for these events, both the BDC and the mixing properties suffer more profound changes in both the middle and the lower stratosphere. The evolution of the PV field during SSWs is analyzed comparing the zonal-mean eddy PV fluxes with the diffusive fluxes in equivalent latitude (i.e., a tracer-based coordinate system necessary for the calculation of the effective diffusivity, Nakamura & Zhu, 2010, and widely used for assessing dynamical and tracer evolutions, e.g., Manney & Lawrence, 2016, and references therein). It is shown that the diffusive fluxes are a simpler diagnostic and capture more details of the PV transport than the zonal-mean PV fluxes, at least under the extreme stratospheric conditions during SSWs.

The remainder of the paper is organized as follows. Section 2 describes the reanalysis and model output used in this study, as well as the diagnostics employed for the estimation of the advective BDC and mixing. Section 3 presents the composite results for reanalysis and WACCM, while section 4 focuses on the different response of transport properties to SSW that are also PJO events in the model. Due to the relevance of PV dynamics for the stratospheric circulation, this section also discusses the redistribution of PV during SSWs. A summary and conclusions are given in section 5.

2. Data and Methods

2.1. Reanalysis and Model Descriptions

In this study we use daily-mean fields from the ERAI for the period 1979–2012 (Dee et al., 2011), with a 1° × 1° longitude-latitude resolution and 60 vertical levels with the top at around 0.1 hPa and a vertical spacing of about 1.5 km in the middle stratosphere. We also use output from four members of an ensemble of 60-year climate runs (i.e., a total of 240 years) using the WACCM version 4. This version of the model has a 2.5° × 1.9° longitude-latitude grid, with the model top at about 140 km altitude. The vertical resolution ranges from 1.1 to 1.4 km in the troposphere and lower stratosphere to 3.5 km in the upper mesosphere and lower thermosphere (Marsh et al., 2013). The latest modifications to the chemistry module and to the orographic gravity wave drag scheme and their combined impact on the Antarctic cold pole bias can be found in Solomon et al. (2015) and Garcia et al. (2017). The simulations used for this study are forced with observed sea surface temperature, solar variability, natural and anthropogenic emissions of greenhouse houses, aerosols, and ozone depleting substances for the period 1955–2014. Each ensemble member only differs in slightly different initial conditions of the atmospheric state.

For the identification of SSWs, we apply the widely used criteria of Charlton and Polvani (2007). Basically, the day when the zonal-mean zonal wind at 60°N and 10 hPa becomes negative defines the central date of an SSW. An event can only be identified as such between November and March (i.e., midwinter warmings), and the minimum separation between two central dates must be longer than 20 days. Besides, if the zonal-mean zonal winds do not return to westerlies for at least 10 consecutive days before 30 April, the event is identified as a final warming and not taken into account as a midwinter SSW. In the 34 year period of ERAI we identify 23 SSWs (0.68 year^{-1}), while in WACCM we have 152 SSWs (0.63 year^{-1}).

Here we provide a brief, qualitative description of the method used to identify PJO events, for a detailed description the reader is referred to Hitchcock, Shepherd, and Manney (2013). The PJO classification is done following Kuroda and Kodera (2004) in terms of the first two empirical orthogonal functions (EOFs) of daily-mean polar-cap-averaged (70°–90°N) temperatures over the middle atmospheric column. Both EOFs present vertical dipoles, the first with maxima in the upper stratosphere and upper mesosphere and the second with maxima in the midstratosphere and mesosphere. A PJO event is identified when the temperature anomaly (as projected onto these two EOFs) maximizes at a height of approximately 60 hPa, so long as it is sufficiently strong. In practice this is determined through the relative phase and amplitude of the principal component time series associated with these two EOFs (see Hitchcock, Shepherd, & Manney, 2013, for details). Consequently, SSWs that occur during PJO will have a strong signal in the lower stratosphere, but note that the identification criteria do not explicitly consider the persistence of the anomalies. When applied to our data we find that 70 SSWs in WACCM and 9 in ERAI occur during PJO events (hereafter PJO-SSW), while 82 SSWs in WACCM and 14 in ERAI are not linked to PJO events (hereafter nPJO-SSW).

2.2. Estimates of Transport and Mixing: Residual Circulation and Equivalent Length

To estimate the changes in the advective Brewer-Dobson circulation, we compute the vertical component of the residual circulation $\bar{w}^*$ under the transformed Eulerian mean formalism:

$$\bar{w}^* \equiv \bar{w} + \frac{1}{a\cos\phi}\partial_\phi\left(\cos\phi\frac{\overline{v'\theta'}}{\partial_z\bar{\theta}}\right). \tag{1}$$

In equation (1), (v, w) are the meridional and vertical wind components, θ is potential temperature, a is the Earth's radius, ϕ is latitude, and z is the log pressure altitude. The overbars denote zonal average, and the primes departure from it.

To estimate the changes in the mixing properties of the flow during SSWs, we evaluate the effective diffusivity (Haynes & Shuckburgh, 2000a; Nakamura, 1996). The effective diffusivity κ_{eff} is a diffusion coefficient that arises from a change of coordinates that preserves the area enclosed by a given tracer contour. The coordinate change assigns the area A enclosed by a tracer contour to a circle of latitude (i.e., the equivalent latitude ϕ_e) that is the boundary of the polar cap with the same area, $A = 2\pi a^2(1 - \sin\phi_e)$ (see Haynes & Shuckburgh, 2000a, for more details). This makes it possible to transform the two-dimensional advection-diffusion equation for a tracer concentration $c(\mathbf{x}, t)$

$$\partial_t c + \nabla(c\,\mathbf{u}) = \nabla\cdot(\kappa\nabla c), \tag{2}$$

into a purely diffusion equation

$$\partial_t C = \frac{1}{a^2\cos\phi_e}\partial_{\phi_e}\left(\cos\phi_e\,\kappa_{eff}\,\partial_{\phi_e}C\right). \tag{3}$$

In equations (2) and (3), $c(\mathbf{x}, t)$ and $C(\phi_e, t)$ are the tracer concentration in geographical and equivalent latitude coordinates, respectively, $\mathbf{u}$ is the horizontal wind vector, and κ is a constant diffusivity coefficient. Based on Nakamura's (1996) study, the effective diffusivity is defined by Haynes and Shuckburgh (2000a) as

$$\kappa_{\text{eff}}(\phi_e, t) \equiv \kappa a^2\frac{\left\langle|\nabla c|^2\right\rangle}{(\partial C/\partial\phi_e)^2}, \tag{4}$$

where the angle brackets represent the area average between consecutive tracer contours. The effective diffusivity quantifies the changes in microscale diffusion due to the large-scale stirring of tracer contours, reflecting the intuition that the elongation of tracer contours leads to an increase in irreversible microscale diffusion across the contour. The diffusivity constant κ, needed for the calculation of κ_{eff}, will depend on the model's spatial resolution and the hyperdiffusivity scheme employed. Since we are interested in quantifying the changes in κ_{eff} associated with SSWs, and not in the absolute values of this variable, we can use the equivalent length L_{eq} (Haynes & Shuckburgh, 2000a):

$$\kappa_{\text{eff}}(\phi_e, t) = \kappa\frac{L^2_{\text{eq}}(\phi_{\text{eq}}, t)}{(2\pi a\cos\phi_e)^2}, \tag{5}$$

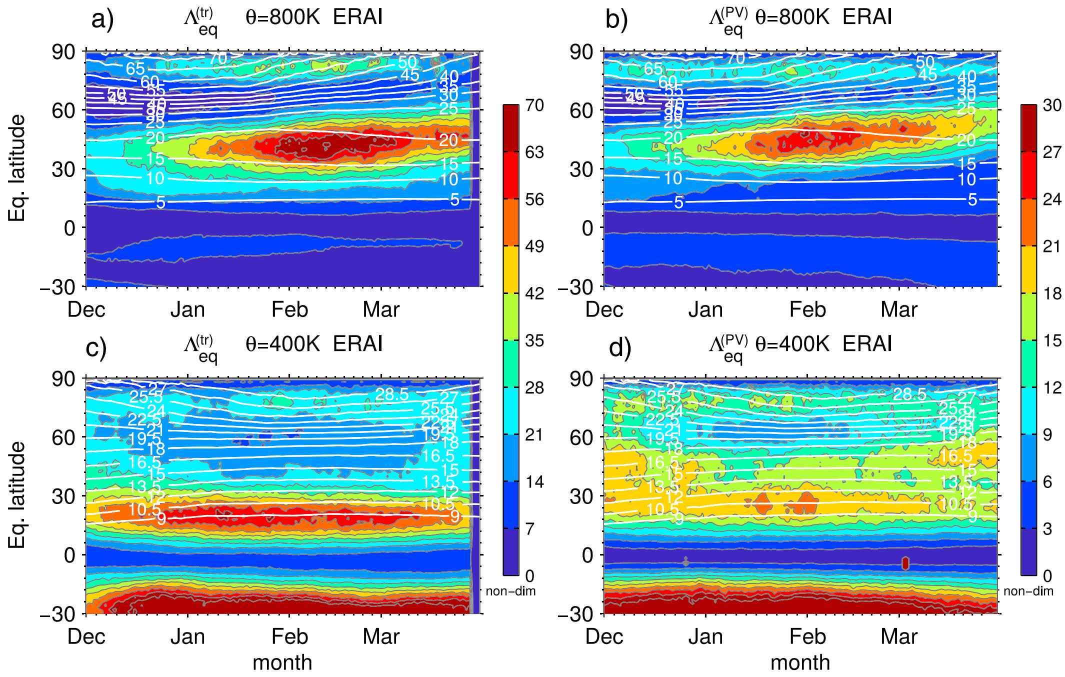

Figure 1. Winter-mean evolution as a function of equivalent latitude of the equivalent length Λ_{eq} (nondimensional) at (a, b) 800 K and (c, d) 400 K, calculated from (a, c) the passive tracer distributions ($\Lambda_{eq}^{(tr)}$), and (b, d) the Eulerian PV fields ($\Lambda_{eq}^{(PV)}$). Solid white lines denote contours of generalized potential vorticity (Müller & Günther, 2003) in equivalent latitude (PVU). European Centre for Medium-Range Weather Forecasts Re-Analysis Interim (ERAI) output for the period 1979–2012.

which provides an upper boundary for the length of the contour corresponding to each tracer value $C(\phi_e, t)$. In particular, we will compute the *normalized equivalent length squared* Λ_{eq}, defined in Shuckburgh et al. (2001) as

$$\Lambda_{eq}(\phi_e, t) \equiv \frac{L_{eq}^2}{(2\pi a \cos\phi_e)^2} \left(= \frac{\kappa_{eff}(\phi_e, t)}{\kappa} \right), \tag{6}$$

which is a nondimensional quantity proportional to the effective diffusivity. To compute Λ_{eq} (hereafter referred to as equivalent length), we need the distribution of a passive tracer $c(\mathbf{x}, t)$ as a function of time, and its transformation to equivalent latitude $C(\phi_e, t)$. Here we briefly compare two methods for the calculation of Λ_{eq}, using ERAI fields. The first integrates the advection-diffusion equation (equation (2)) of an artificial tracer advected by the nondivergent, isentropic winds (see Abalos, Legras, et al., 2016; Abalos, Randel, et al., 2016, for details). The second assumes that the Ertel's PV distribution on isentropes will have a statistically similar distribution to that of a passive tracer in the stratosphere and uses the Eulerian PV fields. Figure 1 compares the northern winter evolution of Λ_{eq} computed from the tracer calculations ($\Lambda_{eq}^{(tr)}$) and from the PV field ($\Lambda_{eq}^{(PV)}$), at the isentropic surfaces of 800 K (~10 hPa) and 400 K (~100 hPa), for ERAI. As noted by Abalos, Legras, et al. (2016), $\Lambda_{eq}^{(tr)}$ is about twice as large as $\Lambda_{eq}^{(PV)}$, which could be due to finer filaments and more detailed structure of the tracer field as compared to the Eulerian PV field. Another factor explaining the contrasting values of both estimates is our use of equations (4) and (6) with the PV field from ERAI. The definition of κ_{eff} is not unique and is based on a passive tracer that responds to equation (2). This is not directly applicable to PV in ERAI (and WACCM) because a fourth-order hyperdiffusion scheme is used to dissipate the small-scale enstrophy generated by geostrophic turbulence. The hyperdiffusion modifies equation (4), which will contain higher-order derivatives of $c(\mathbf{x}, t)$ as presented by Nakamura and Zhu (2010): $\kappa_{eff}^{(4)} \equiv \kappa^{(4)} a^2 \left\langle \nabla(\nabla^2 c) \cdot \nabla c \right\rangle / (\partial C / \partial \phi_e)^2$. However, we see in Figure 1 that $\Lambda_{eq}^{(tr)}$ and $\Lambda_{eq}^{(PV)}$ present good qualitative agreement. At 800 K (Figures 1a and 1b), the region of strong PV gradients (ϕ_e ~ 60°N) presents a minimum of Λ_{eq}, evidencing the transport barrier at the vortex edge. There are larger values of Λ_{eq} on both sides of the vortex edge, particularly in the region from $\phi_e = 30°$N to 55°N (i.e., the surf zone), that intensify in January as the PV gradients at the vortex edge sharpen. At 400 K, there is enhanced mixing over a band south of $\phi_e = 30°$N in both estimates (although relatively stronger in $\Lambda_{eq}^{(tr)}$), probably due to wave breaking in the upper flank of the tropospheric subtropical jet. However, the region of enhanced $\Lambda_{eq}^{(PV)}$ in the subtropics in December and March extends farther north (up to ∼55°N) than in the case of $\Lambda_{eq}^{(tr)}$. There is also a band of strong mixing in the subtropics over the southern subtropical jet. In this case, the values of Λ_{eq} are larger than their northern counterpart due to the presence of the zero-wind line in the summer hemisphere near 400 K and 30°S, which reinforces the breaking—and subsequent stirring and mixing—of stationary Rossby waves (see Abalos, Legras, et al., 2016). At midlatitudes near 60°N there is a relative minimum of Λ_{eq}, coinciding with the strong PV gradients at the bottom of the polar vortex.

The similarity between the two estimates of Λ_{eq} justifies our choice of using the PV field in this study, as the integration of the advection-diffusion equation for 240 years of WACCM output is very expensive computationally. It also validates our choice of using equations (4) and (6) to derive Λ_{eq} from PV, since we are interested in relative changes to this magnitude during SSWs. Although we might be underestimating the absolute value of mixing by not taking into account the model's hyperdiffusivity, we do not expect structural differences when computing anomalies during SSWs. And with this choice, we avoid further problems with numerical noise from the calculations of high-order derivatives. In addition, the mixing properties derived from the PV field are also of intrinsic interest since PV dynamics are crucial to the circulation of the middle atmosphere. Therefore, in the next sections we will show composites of Λ_{eq} derived from the PV field using equations (4) and (6) for both ERAI and WACCM.

The composite plots of the various anomaly fields presented in the remainder of the paper are calculated first by subtracting the daily climatological average from the daily value and then compositing them about the SSW central date. We have used all the years available to compute the climatologies, thus including years with SSWs. Although this is a common methodology (e.g., Charlton & Polvani, 2007), note that the anomalies would likely be larger if computed relative to non-SSW years. The statistical significance of the composite plots is assessed applying a two-tailed Student's t test with $N - 1$ degrees of freedom, N being the number of SSWs included in the composite and a confidence level of 99% (i.e., $\alpha = 0.01$). Each SSW event has been assumed to be independent to estimate the degrees of freedom.

3. Transport and Mixing During SSW Events

3.1. The Residual Circulation

Figure 2 shows the composite evolution of several relevant variables averaged longitudinally (zonal wind averaged over 60°–70°N, temperature, potential temperature, and diabatic heating anomalies averaged north of 70°N, and Eliassen-Palm (EP) flux divergence anomalies averaged over 45°–75°N) as a function of time with respect to the central date of the SSW and pressure, in ERAI and WACCM. The various anomaly fields shown in this paper, if not stated otherwise, have been standardized by dividing by the daily climatological standard deviation, σ, at each vertical level to highlight the relative importance of the anomalies at different altitudes. We first focus on the reanalysis (top row in Figure 2). The anomalies of EP flux divergence are negative during at least 30 days before the SSW, contributing to a gradual deceleration of the westerly jet and the warming of the polar stratosphere. Near lag 0 the anomalous wave forcing is stronger than 0.6σ between 30 and 0.3 hPa (peak of 0.9σ around 1 hPa), easterly winds appear in the middle-to-upper stratosphere and the polar warming intensifies. After the central day of the warming the wave forcing weakens, and the winds and temperature recover at a much faster rate in the upper stratosphere than lower down due to differences in radiative timescales at different altitudes (Hitchcock, Shepherd, Taguchi, et al., 2013). Evidence of this behavior is shown in the evolution of radiative heating anomalies Q at polar latitudes (Figures 2c and 2f). Before the SSW, the polar stratosphere is warmed adiabatically and the radiative heating anomalies are negative throughout the stratosphere, especially in the upper stratosphere. The Q anomalies change sign in the upper stratosphere (5–1 hPa) right after lag 0, whereas the negative anomalies last up to 3 months below 100 hPa, with intensities exceeding -0.6σ until lag 45. The general evolution of these fields in ERAI and WACCM is very similar, although the composites are smoother in the model partly due to the larger number of SSW events.

Figure 3 shows the anomalies of the polar downwelling and tropical upwelling, composited about the central date of SSW in ERAI and WACCM. To reduce the quasi-biennial oscillation signal, we have removed the 61-day average around the SSW date for each SSW, following Kodera (2006) and Gómez-Escolar et al. (2014). Focusing on ERAI (Figure 3, left column), the residual circulation accelerates preceding the SSW central date, with negative $\bar{w}^*$ anomalies in the polar region (stronger downwelling) and positive anomalies over the tropics (stronger upwelling). This strong downwelling ultimately drives the adiabatic warming of the polar stratosphere during

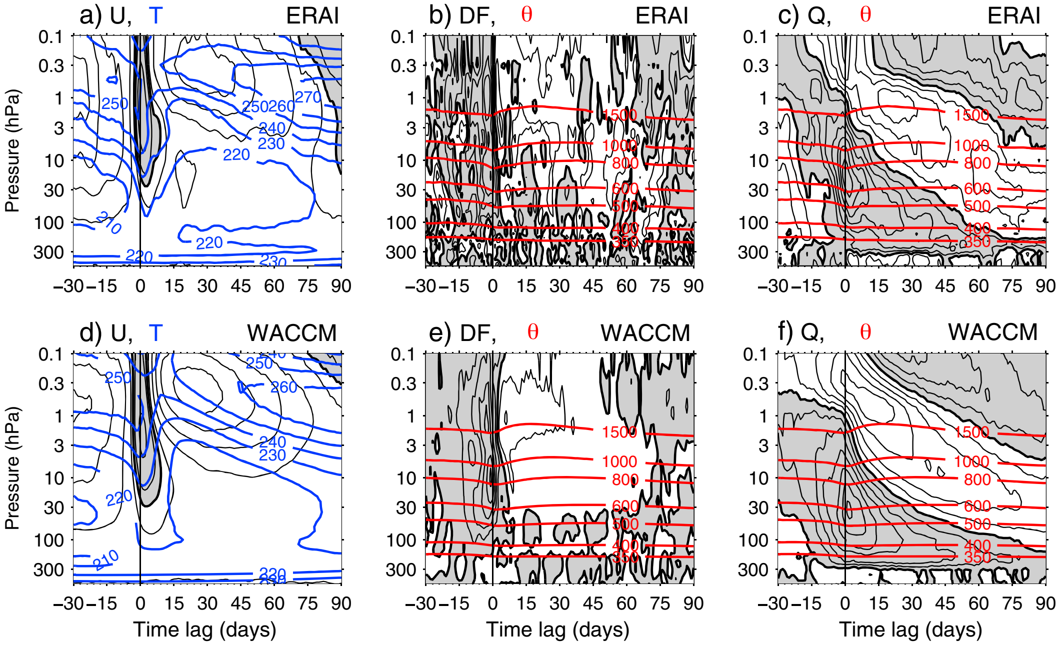

Figure 2. Composite evolution about the central sudden stratospheric warmings date as a function of height of (a, d) zonal-mean zonal wind from 60°N to 70°N (black contours at 10 m/s intervals starting at ±5 m/s; zero contour is thick), and polar cap temperature north of 70°N (blue contours at 10 K intervals); (b, e) standardized anomalies of the EP flux divergence from 45°N to 75°N (black contours at 0.3σ intervals; zero contour is thick) and polar cap potential temperature (red contours at 350, 400, 500, 600, 800, 1,000, and 1,500 K from bottom to top); and (c, f) standardized anomalies of the diabatic heating Q averaged north of 70°N (black contours at 0.3σ intervals; zero contour is thick), for (a–c) European Centre for Medium-Range Weather Forecasts Re-Analysis Interim (ERAI) and (d–f) Whole Atmosphere Community Climate Model (WACCM). Negative values for the variables displayed in black contours are shaded in gray.

the onset of the SSW (e.g., Hitchcock & Shepherd, 2013; Limpasuvan et al., 2012; Matsuno, 1971). Although the alterations to $\bar{w}^*$ in the tropics and high latitudes are consistent, the relative intensity is different. The peak of the anomaly reaches -1.2σ at 100–3 hPa in the polar region, while it reaches 0.9σ at the 20–3 hPa over the tropics. Of course, this does not imply that changes in tropical mass upwelling are inconsistent with the changes in polar mass subsidence (we have checked that they are consistent indeed), but only that the intensity of the $\bar{w}^*$ anomaly with respect to the interannual variability in each region is larger in high latitudes than in the tropics. The sign of the circulation anomalies reverses almost simultaneously at all stratospheric levels, and there is an extended period of time of about 2 months after the central date with weaker meridional circulation. This is qualitatively consistent with the positive EP flux divergence anomaly at midlatitudes present during this period (Figure 2a).

The meridional circulation changes linked to SSW events are well captured in the model (Figure 3, right column). The results are similar to ERAI in timing and vertical structure, but the overall patterns are smoother and the signal is more robust statistically due to the larger sample of SSWs. In particular, the extended period of weaker BDC circulation in the aftermath of the SSW is statistically significantly longer in the lower than in the upper stratosphere, both at polar and tropical latitudes. This is likely due to the longer radiative relaxation timescales in the lower stratosphere (Dickinson, 1973; Randel et al., 2002). In the context of sufficiently deep SSWs (in particular, those SSWs that are followed by PJO events), Hitchcock and Shepherd (2013) showed that the combination of the wave driving suppression and the slow radiative damping in the aftermath of those SSWs caused weaker than normal polar downwelling (i.e., positive anomalies of $\bar{w}^*$) for more than 2 months. We will see in section 4 that this signal in the lower stratosphere in WACCM is dominated by SSWs also categorized as PJO events, both in the tropics and extratropics.

3.2. Isentropic Mixing

Figure 4 shows the standardized anomalies of equivalent length (Λ_{eq}, in color shading), as a function of time and equivalent latitude, composited about the central warming date at several isentropic surfaces, for both ERAI and WACCM. Also shown in this figure is the composite evolution of the generalized PV field

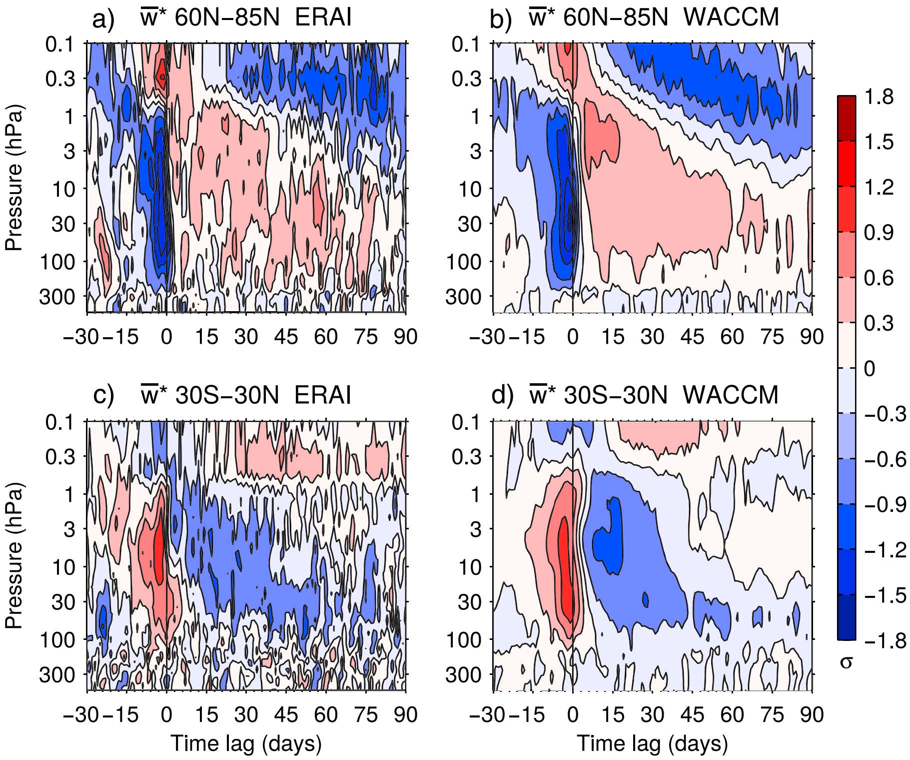

Figure 3. Composites about the central warming date of $\bar{w}^*$ standardized anomalies as a function of time lag and height, averaged over (a, b) the polar region (60°N–85°N, polar downwelling) and (c, d) the tropical region (30°S–30°N, tropical upwelling), for (a, c) ERAI, and (b, d) WACCM. Absolute values larger than 0.5σ for ERAI and 0.2σ for WACCM are statistically significant (Student's t test, $\alpha = 0.01$).

(Müller & Günther, 2003) for the same period (thick black contours). Focusing on the reanalysis results (Figure 4, left column), a strong increase in mixing takes place around and after the central date of the warming around $\phi_e = 60$°N. At 800 K (Figure 4a) the anomalies appear around lag 0 and $\phi_e = 40°–60°$N, on the southward flank of the strong PV gradients that signal the location of the vortex edge. These positive Λ_{eq} anomalies migrate up the PV gradient with time as the PV gradients weaken and the vortex shrinks, reach their maximum ($>1.8\sigma$) at lags 5–15 and $\phi_e = 65$°N and vanish more than 1 month after the SSW central date. As the region of enhanced mixing migrates up the PV gradient after the SSW central date, an area of negative Λ_{eq} anomalies appears at lower equivalent latitudes at lag 20 and moves up gradient as the PV gradients regain intensity around 2 months after the warming. This anomalous pattern of Λ_{eq} signals a poleward (in ϕ_e coordinates) shift with respect to the climatological configuration (Figure 1b). At lower stratospheric levels, the mixing anomalies appear and vanish later. For example at 400 K, near the base of the vortex, the significant positive anomalies of Λ_{eq} do not appear until 2 weeks after the SSW central day and disappear 2 months after the SSW central date. There are also 1σ anomalies in the equivalent length over an area equal to the polar cap northward of 60°N that is occurring in a layer below the vortex at 350 K. These anomalies are not associated with the tropopause (as can be inferred from the PV contours in Figure 4i) but rather occur within the lowermost stratosphere.

The behavior of the mixing properties during SSWs is similar in WACCM (Figure 4, right column); strong positive anomalies appear at upper levels first, shift up gradient with time, and last around 30 days at 800 K and around 60 days at 400 K. The overall evolution of both Λ_{eq} and PV is again smoother in the model than in ERAI, which may result from a combination of working with a much larger sample of SSWs in the model composite, and weaker climatological PV gradients in the WACCM. The large positive anomalies of Λ_{eq} in the stratosphere (i.e., enhanced mixing) in both the reanalysis and the model are a result of the intensified wave breaking that occurs prior to and a few days after the central date of the warming (Figures 2a and 2b) and the associated chaotic advection and irreversible deformation of PV contours at the vortex edge that enhance the microscale diffusion (Nakamura, 1996). Following this reasoning, the band of negative anomalies in mixing properties

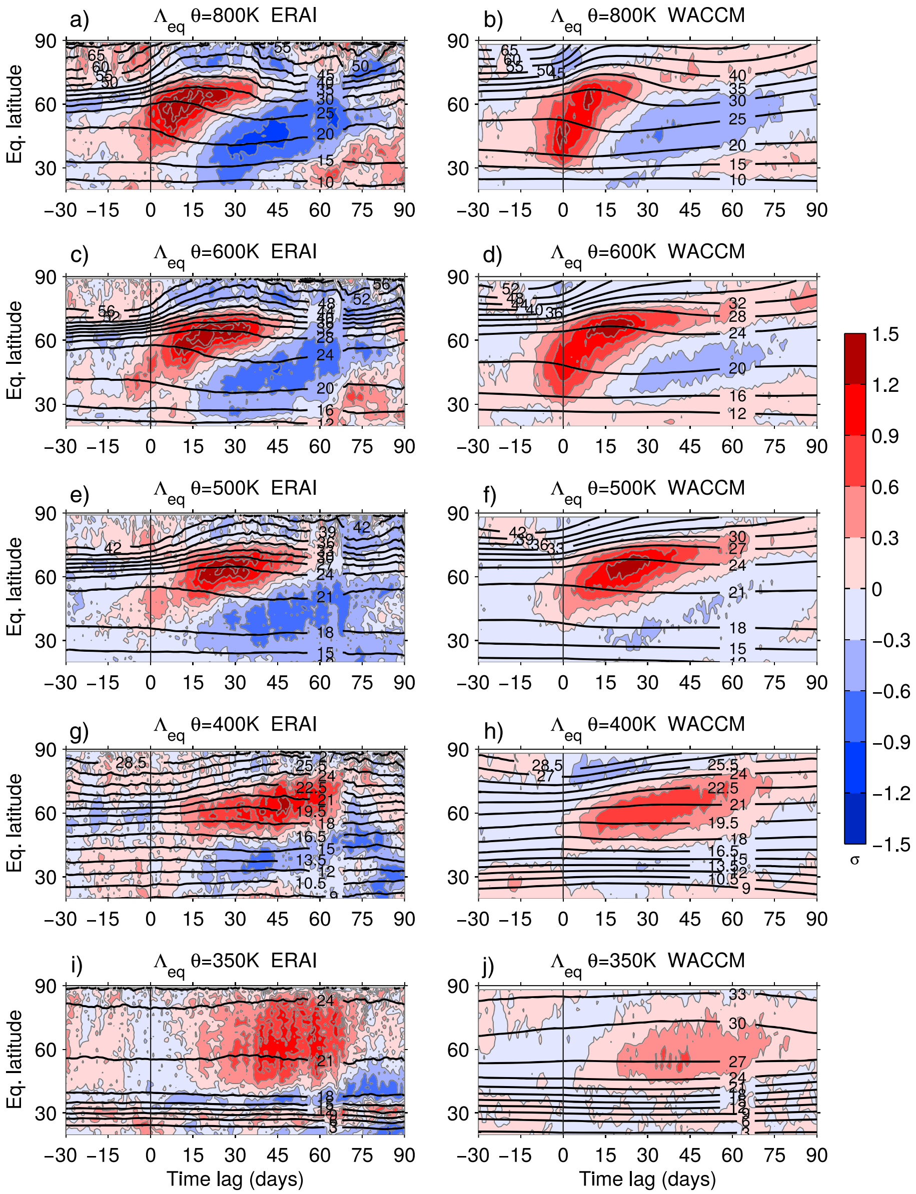

Figure 4. Composites of standardized anomalies of Λ_{eq} as a function of time lag and equivalent latitude for (left column) ERAI and (right column) WACCM, at the (a–b) 800, (c–d) 600, (e–f) 500, (g–h) 400, and (i–j) 350 K isentropic surfaces. Absolute values larger than 0.5σ for ERAI, and 0.2σ for WACCM, are statistically significant (Student's t test, $\alpha = 0.01$). Contours are generalized potential vorticity isolines (PVU).

in the midstratosphere is linked to the suppression of wave activity and forcing in the aftermath of the warming (Figures 2a and 2b), which contributes to the vortex regeneration.

The WACCM runs capture quite reliably the changes in the advective BDC and isentropic mixing associated with sudden stratospheric warmings, as compared to ERAI (at least in a qualitative sense). This allows us to further explore in the next section the driving mechanisms and consequences of the abovementioned transport and mixing changes using WACCM, where the large sample of SSWs provides the statistical robustness that the reanalysis lacks.

4. Modulation of Transport and Mixing by PJO Events

4.1. Residual Circulation and Isentropic Mixing

Figure 5 shows the composite evolution of the same variables displayed in Figure 2, but this time grouping the SSWs that are also PJO events (PJO-SSW) and those that are not PJO events (nPJO-SSW), in WACCM.

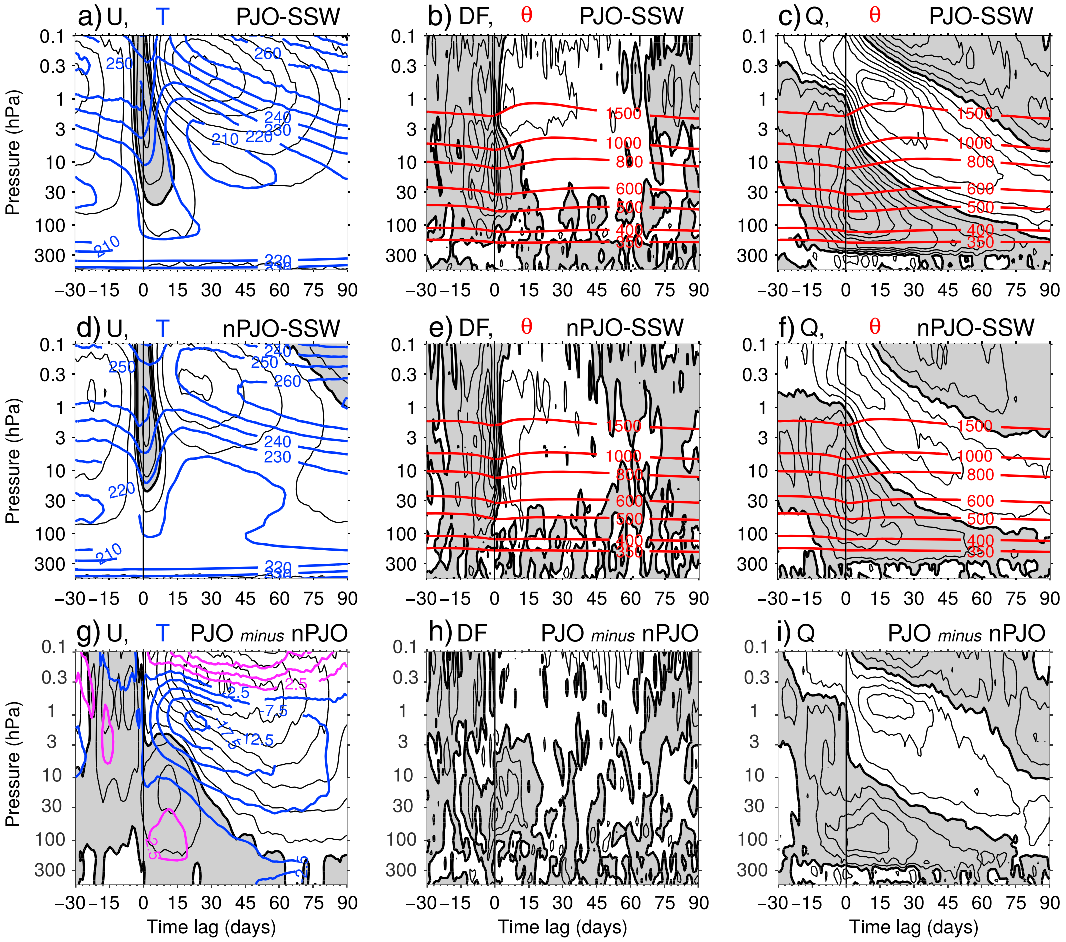

Figure 5. (a–c and d–f) As in Figure 2 but for composites of Polar-night Jet Oscillation-sudden stratospheric warming (PJO-SSW) and non-PJO SSW (nPJO-SSW) in WACCM. (g–i) Difference between PJO and nPJO events. In (g), zonal-mean wind isolines (black contours) are at 5 m/s intervals starting at ±2.5 m/s; zero contour is thick); positive *T* differences are in magenta and negative are in blue, at 5 K intervals starting at ±2.5 K.

Besides, the bottom row in Figure 5 shows the difference between PJO and nPJO events. As expected, the circulation and temperature changes for PJO-SSW events have a deeper penetration into the lower stratosphere than for nPJO-SSWs. The anomalous wave forcing is stronger and lasts longer in the lower stratosphere in PJO events than in nPJO events (there are negative anomalies that persist over a week after the central warming date; see Figure 5h), and consequently, the easterlies and the initial warming reach lower altitudes in the former than in the latter (Figure 5g). Also, the upper stratospheric winds and temperature recover faster in PJO-SSW events, with an apparent downward propagation. Hitchcock and Shepherd (2013) showed that this apparent propagation is in reality a result of much faster radiative timescales in the upper than in the lower stratosphere. We see in Figure 5c that for PJO-SSWs, the anomalies in the diabatic heating Q maximize below 30 hPa, while for nPJO-SSWs the peak of the anomaly is located above 30 hPa. Also, the maximum anomaly is stronger for PJO than for nPJO, 2.1σ versus 1.5σ.

Figure 6 shows the anomalies in polar downwelling and tropical upwelling as a function of pressure and time with respect to the SSW central day, for PJO-SSW and nPJO-SSW events in WACCM. At negative lags there is not much of a difference between the two types of SSW, except that the anomalous strengthening of the circulation starts about a week earlier in PJO events. But the vertical extent of the circulation strengthening, and the magnitude of the strengthening itself, is similar in both latitude bands prior to the central date in each composite. The most obvious difference is the duration of the anomalously weak circulation in the aftermath. While the statistically significant anomalies disappear after lag 45 in nPJO-SSWs, they last 90 days below 30 hPa in PJO-SSW events. And this happens consistently in polar latitudes and the tropics. To our knowledge, this connection between PJO-SSW events and persistent weak upwelling in the tropics had not been

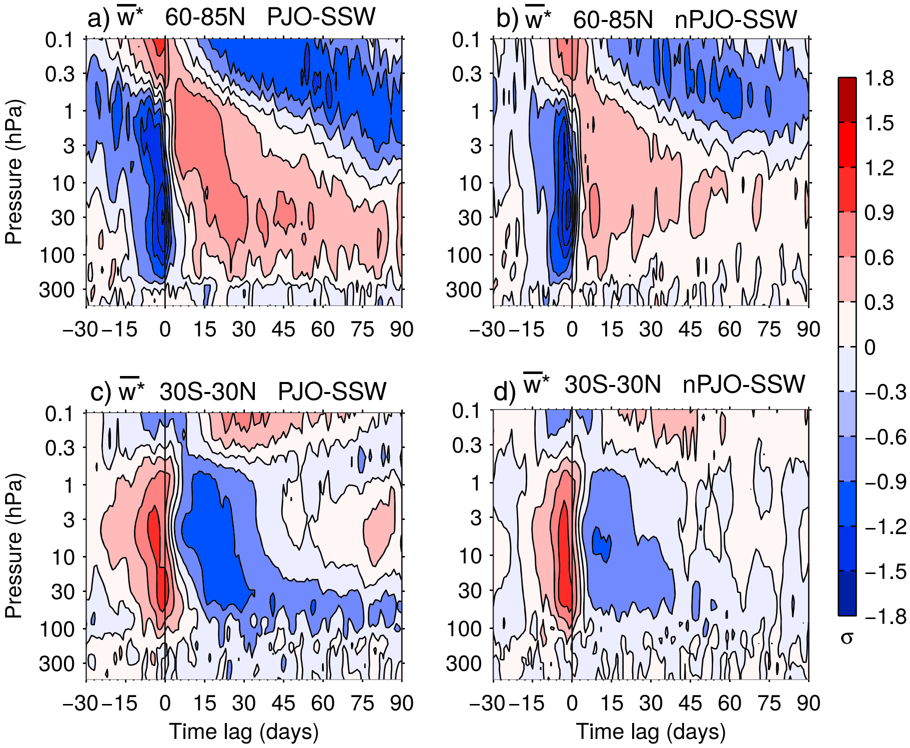

Figure 6. As in Figure 3 but for composites of Polar-night Jet Oscillation-sudden stratospheric warming (PJO-SSW) and non-PJO SSW (nPJO-SSW) in WACCM. Absolute values larger than 0.3σ are statistically significant (Student's *t* test, $\alpha = 0.01$).

noticed before. It is oftentimes assumed that the BDC is stronger in winters with SSWs (Abalos et al., 2015; Tao et al., 2015). This may be the case close to the SSW onset, but there are anomalies of both signs before and after SSWs and the effect on seasonal estimates of the BDC is not straightforward. It may depend (among other factors) on the vertical level and the type of SSW (PJO versus nPJO).

Figure 7 shows composites of the evolution of Λ_{eq} anomalies as a function of equivalent latitude ϕ_e for PJO-SSW and nPJO-SSW in WACCM, at different isentropic levels. The overall patterns are similar to those shown in the right column of Figure 4. Enhanced mixing properties appear in the midlatitudes around lag 0 as the PV gradients at the vortex edge weaken and migrate poleward, evidencing the sudden reduction of the size of the vortex. At all isentropic levels shown in Figure 7, the composite for PJO-SSW events shows stronger anomalies that last longer than those in the composite for nPJO-SSW events. And the evolution of PV is also more abrupt in PJO-SSW events, particularly at the 800 and 600 K levels. In the lower stratosphere (350−400 K), large Λ_{eq} anomalies are present in the PJO composite consistent with longer perturbations of the lower stratosphere in PJO events, while the nPJO-SSWs present much weaker anomalies at these altitudes. This behavior of the mixing is consistent with what it is known of PJO events, with a more intense wave forcing that drives a profound circulation and temperature response (e.g., Hitchcock & Shepherd, 2013).

4.2. Isentropic Redistribution of Potential Vorticity

The difference in mixing properties between PJO-SSW and nPJO-SSWs has interesting consequences for the PV transport after the central SSW date. To study this in more detail, we compute the *diffusive flux* of PV (F_d) in equivalent latitude coordinates (see equation 2.9 in Nakamura, 1996):

$$F_d(\phi_e, t) = -\frac{\kappa_{\text{eff}}(\phi_e, t)}{a \cos \phi_e} \partial_{\phi_e} P_e(\phi_e, t), \tag{7}$$

where P_e is PV in equivalent latitude coordinates. Following Nakamura (1996), the diffusive flux gives the rate of circulation change around the PV contour enclosed by the equivalent latitude ϕ_e, and it is equivalent to the dissipation of pseudomomentum due to diffusion integrated around the PV contour. By definition total F_d

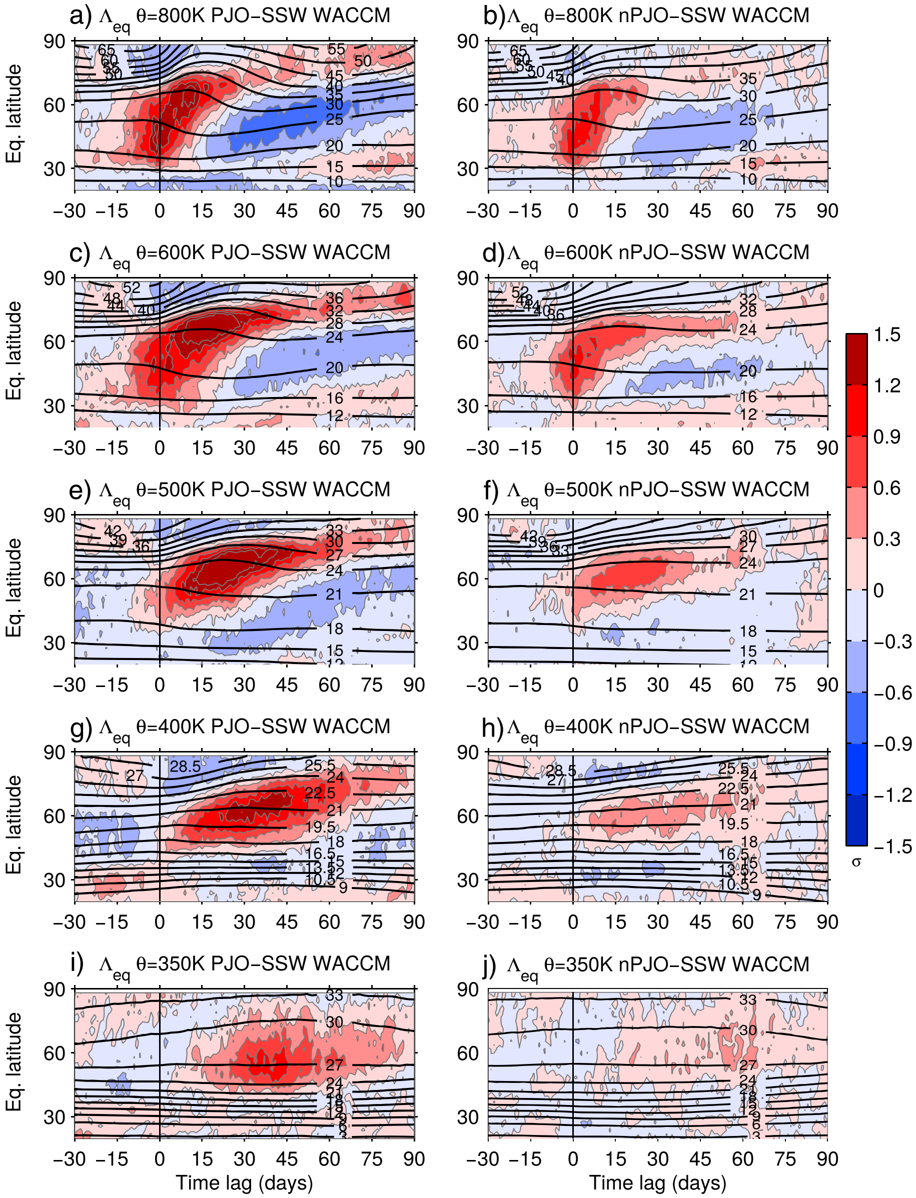

Figure 7. As in Figure 4 but for composites of Polar-night Jet Oscillation-sudden stratospheric warming (PJO-SSW) and non-PJO SSW (nPJO-SSW) in WACCM. Absolute values larger than 0.3σ are statistically significant (Student's t test, $\alpha = 0.01$).

is directed down gradient. Since the contours of PV in equivalent latitude are themselves advected by the winds, the PV flux has no advective term by the horizontal flow in this coordinate system. Note that in addition to the divergence of the diffusive flux F_d, there will be diabatic terms in the PV evolution equation in equivalent latitude coordinates. Since we are interested in changes of F_d during SSWs (and not in its absolute magnitude), we use Λ_{eq} instead of κ_{eff} in equation (7) to compute F_d, as Λ_{eq} and κ_{eff} only differ in a constant diffusivity coefficient κ (see equation (6)). Again, as in all previous plots, the standardized anomalies give a measure of the relative importance of the anomalies at each vertical level.

Figure 8 displays the composite evolution of F_d anomalies for PJO-SSW and nPJO-SSW events in WACCM and the cyan curve represents the approximate location of the vortex edge calculated as the location of the maximum gradient of PV in equivalent latitude coordinates (e.g., Lawrence & Manney, 2018). The pattern of anomalous F_d at 800 K is qualitatively similar for PJO-SSW and nPJO-SSW (Figures 8a and 8b), although the anomalies are generally stronger and last longer in the former than in the latter, consistent with

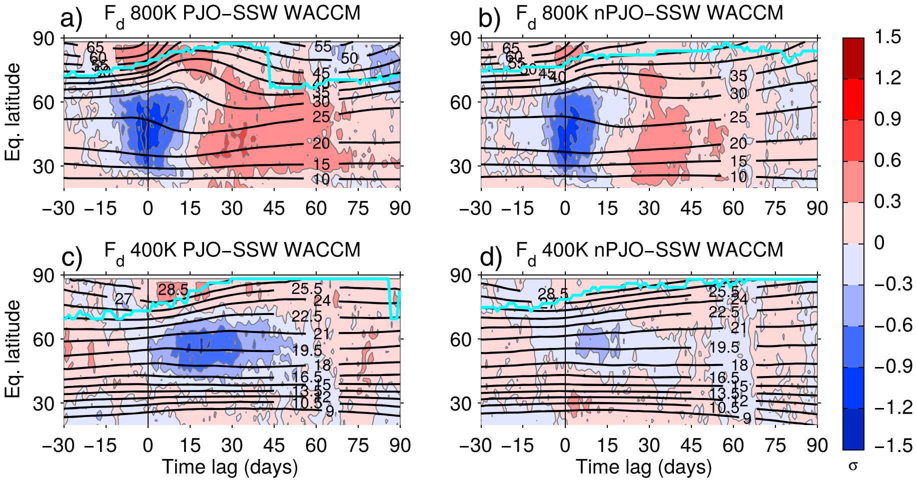

Figure 8. Composites of standardized anomalies of the diffusive potential vorticity flux (F_d) as a function of time lag from the SSW central date and equivalent latitude, for (a, c) PJO-SSWs and (b, d) nPJO-SSWs, at 800 and 400 K isentropic surfaces. Absolute values larger than 0.3σ are statistically significant (Student's t test, $\alpha = 0.01$). The black contours are the generalized potential vorticity in equivalent latitude (in PVU), and the cyan contour represents the approximate location of the edge of the vortex (see text).

the evolution of Λ_{eq} (Figure 7). The patterns present a dipolar structure in equivalent latitude characterized by negative anomalous PV fluxes to the south and positive anomalous fluxes to the north of $\sim \phi_e = 65°$N from lag −10 to about lag +15 days, which roughly coincides with the approximate location of the vortex edge. After lag 15, weak negative anomalies dominate north of 25°N. This evolution of diffusive PV flux is reflected on the evolution of the PV contours in both composites (black lines in Figure 8), which bend in the direction of the anomalous flux. In particular, the dipolar structure around lag 0 contributes to the shrinking of the vortex and weakening of the PV gradients at its edge, while the positive anomalous fluxes in the aftermath contribute to the regeneration of the gradients. This vortex regeneration is more evident in the case of PJO-SSW events, where the equivalent latitude of maximum PV gradient jumps abruptly at lag 45 from $\phi_e \sim 85°$N to ~65°N, a position much closer to normal conditions (Figure 7a).

The evolution of the anomalies is rather different between PJO-SSW and nPJO-SSW at 400 K compared to 800 K. Since PJO events are characterized by persistent anomalies at those altitudes (although this is not a prerequisite for their identification), there are relatively strong F_d anomalies (up to -0.9σ) at 400 and 350 K (not shown) that are not present in the nPJO composite, consistent with the anomalous pattern of Λ_{eq} in Figure 7. At 400 K (Figure 8c), there is a similar dipolar structure approximately about the vortex edge to that at 800 K, but it only appears during the first week after the SSW central date and has weaker relative amplitude. The negative anomalies at $\phi_e = 45°–65°$N are present from lag 0 to 45, with maximum amplitude ($> 1\sigma$) at around lag 20. The situation is similar at 350 K (not shown), but the negative fluxes are present from lag 15 to 60 and located further south with a maximum around $\phi_e = 50°$N.

This behavior in the lower stratosphere for PJO events, with significant negative anomalies of diffusive fluxes of PV in the midlatitudes for an extended period of time, acts against the recovery of the vortex to its climatological winter conditions. Indeed, an anomalously negative flux of PV tends to decelerate the winds and weaken the PV gradients at the vortex edge. At 400 K (the base of the polar vortex), the weakening of those gradients does not happen until the negative F_d anomalies appear. From this perspective, it is very similar to what happens at 800 K but shifted in time and at a slower rate. This is somewhat unexpected from the zonal-mean transformed Eulerian mean diagnostics, which show no enhanced wave driving and thus no enhanced eddy advective fluxes across latitude circles at this height and time in the recovery (we will analyze this in more detail in Figure 10 below). To provide a qualitative understanding of the differences in F_d between PJO and nPJO in the lower stratosphere, the top row of Figure 9 presents a couple of daily PV maps at 400 K showing the 21 PV units (PVU, 1 PVU = 10^{-6} m s^{-1} K kg^{-1}) isopleth for a particular PJO-SSW event at lag 0 and lag 21 d. This PV contour encloses approximately the same area as the polar cap north of 60°N, as we see in Figure 8c. At lag 0 (Figure 9a) the PV contour is relatively close to zonal symmetry, and the anomalies

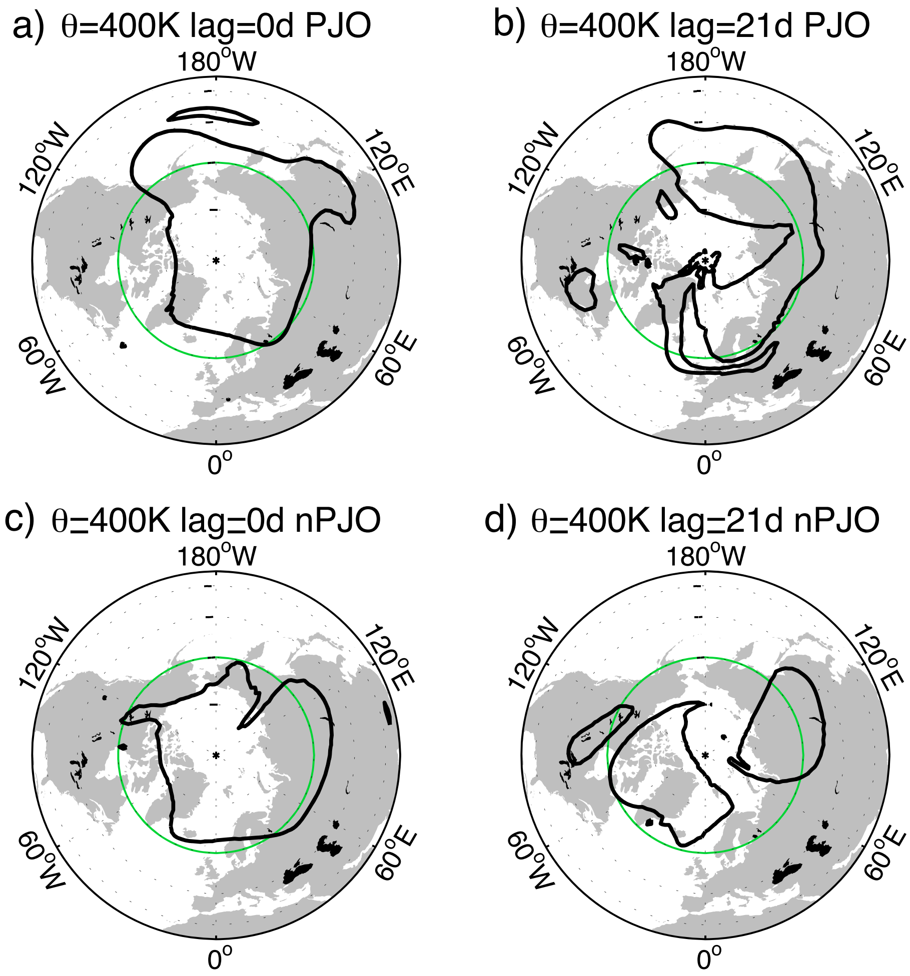

Figure 9. Generalized potential vorticity maps at 400 K (orthographic projection) showing the 21 PVU isopleth (black contour), which approximately encloses the area equivalent to that enclosed by the parallel 60°N (green contour). Potential vorticity maps (a and b) for a Polar-night Jet Oscillation-sudden stratospheric warming (PJO-SSW) case at (a) lag 0, and (b) lag 21, and (bottom row) for a non-PJO SSW (nPJO-SSW) event at (c) lag 0 and (b) lag 21.

of F_d are not statistically significant (Figure 8c). But at lag 21 (Figure 9b), we clearly see the correspondence between an extreme elongation of the PV contour and the enhancement of both Λ_{eq} (Figure 7g) and the diffusive flux (Figure 8c). The bottom row displays similar maps at the same time lags but for a nPJO-SW event. Much less elongation of the PV contour at lag 21, compared to the PJO event, translates into smaller anomalies of both Λ_{eq} (Figure 7h) and F_d (Figure 8d).

It is useful to compare the evolution of the diffusive fluxes with the eddy PV fluxes that arise from the zonal-mean equation of PV. Consider the isentropic PV equation in flux form (Haynes & McIntyre, 1987)

$$\partial_t(\sigma_\theta P) = \frac{1}{a\cos\phi}\left\{\partial_\lambda\left[\sigma_\theta u P + Q\partial_\theta v - Y\right] + \partial_\phi\left[\left(\sigma_\theta v P - Q\partial_\theta u + X\right)\cos\phi\right]\right\}, \tag{8}$$

where P is Ertel's PV, $\sigma_\theta \equiv -g^{-1}\partial_\theta p$ is the isentropic density (g is gravity acceleration and p is pressure), Q is the diabatic heating rate (i.e., vertical velocity in isentropic coordinates), and (X, Y) the horizontal components of some body force. The tendency of PV is given by the divergence of a vector in the horizontal plane. Haynes and McIntyre (1987, 1990) provided discussions on the conservation properties of PV and the similarities and disparities with chemical tracers. Taking the zonal mean of equation (8) yields

$$\partial_t\overline{(\sigma_\theta P)} = \frac{1}{a\cos\phi}\partial_\phi\left[\cos\phi\left(\overline{\sigma_\theta v P} - \overline{Q\partial_\theta u} + \bar{X}\right)\right]. \tag{9}$$

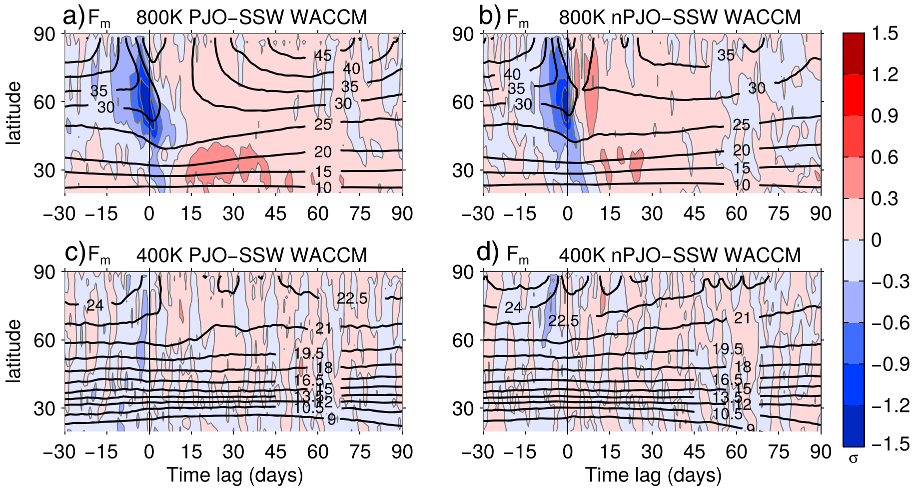

Figure 10. Same as Figure 8 but for the zonal-mean eddy potential vorticity flux F_m. Absolute values larger than 0.3σ are statistically significant (Student's t test, $\alpha = 0.01$). The black contours are the zonal-mean generalized potential vorticity (in PVU). PJO-SSW = Polar-night Jet Oscillation-sudden stratospheric warming; nPJO-SSW = non-PJO SSW.

The terms on the right-hand side of equation (9) can be decomposed into an advective part of the zonal-mean fields, and an eddy flux component given by

$$F_m = \bar{\sigma}_\theta \overline{\hat{v}\hat{P}}^{*},\; F_Q = -\bar{\sigma}_\theta \overline{\hat{Q}(\partial_\theta \hat{u}/\sigma_\theta)}^{*}. \tag{10}$$

Here we have used the following the notation in isentropic coordinates: $\bar{b}^* \equiv \overline{\sigma_\theta b}/\bar{\sigma}_\theta$ and $\hat{b} \equiv b - \bar{b}^*$, b being any variable. F_m represents the meridional eddy PV flux and F_Q the "diabatic eddy PV flux," which redistributes PV latitudinally due to diabatic effects. We will compare F_d with the meridional eddy PV flux F_m, which reflects our intuition that there should be some connection between the eddy PV fluxes across latitude circles and the diffusive flux of PV across equivalent latitude lines, since the effective diffusivity (or the equivalent length) indeed shows that large-scale stirring enhances mixing (Nakamura & Zhu, 2010, proposed a formalism for finite amplitude eddy-mean flow interaction for barotropic flows, in equivalent latitude coordinates, and discussed the effects of diffusive and advective PV fluxes on the evolution of a finite amplitude wave activity). Figure 10 displays similar plots to those in Figure 8 but for F_m. In the isentropic formulation the eddy PV flux is not exactly equal to the EP flux divergence, as happens in the quasi-geostrophic theory, but we can still see similarities between Figure 10 and the EP flux divergence in Figures 5b and 5e. At 800 K, there are negative anomalies of F_m north of 40°N from around lag −15 to about lag 0 acting to smooth out the structure of elevated PV over the pole; the anomalies start a bit earlier and last a few days longer after the SSW in the case of PJO-SSWs as compared to nPJO-SSWs. After this the anomalous fluxes are positive for both types of SSWs, but no statistically significant signal is captured. At 400 K (Figures 10c and 10d) there are weak negative fluxes right before lag 0 that are barely significant, and no signal corresponding to the strongly enhanced diffusive fluxes can be seen for either PJO-SSW and nPJO-SSW events.

There are some qualitative similarities between F_d and F_m in Figures 8 and 10, respectively, such as the change of sign the anomalies at 800 K soon after the central warming date for both fields. But there are also noticeable differences, such as the absence of statistically significant anomalies of F_m at 400 K, and the ability of the ϕ_e coordinate to better distinguish between inside and outside the vortex. Note that the intensity of the vortex is also better captured in the ϕ_e framework: at 800 K (400 K) we are able to capture the 65(28.5) PVU isopleth in ϕ_e (Figure 8), while the largest value shown in the zonal-mean perspective is the 45 (26.5) PVU (e.g., Figure 10). Due to these qualities of the equivalent latitude framework, we can distinguish a dipole of positive and negative diffusive flux anomalies at both sides of the vortex edge around lag ±15 d that is not present in the zonal-mean fluxes.

Although there exists a connection between Rossby wave breaking and large-scale stirring and mixing, the PV fluxes represented by F_d and F_m are manifestly different during the recovery period after SSWs. It is beyond the scope of this study to evaluate the balance of PV and fully understand this difference, but we suggest that it is likely explained by diabatic effects and the decay of wave activity in this period (Haynes & McIntyre, 1987; Nakamura & Zhu, 2010).

5. Summary and Conclusions

We have studied the changes in transport and mixing properties of the stratospheric flow due to the occurrence of SSWs in ERAI (1979–2012 period) and the chemistry climate model WACCM (four 60-year runs, a total of 240 years). We have evaluated (1) the vertical component of the residual circulation to look at the changes in the advective transport and (2) the normalized equivalent length squared Λ_{eq}, which is proportional to the effective diffusivity (see Haynes & Shuckburgh, 2000a; Nakamura, 1996), to analyze changes in the mixing properties of the flow.

To our knowledge, this study presents the first analysis of the composite changes of these properties using reanalysis and long model runs. Our main findings include (i) a weakened residual circulation and intensified isentropic mixing after the onset of SSWs that persist for more than 2 months in the lower stratosphere, (ii) sufficiently deep SSWs (in particular those followed by PJO events) have a stronger and more persistent response in the meridional circulation and isentropic mixing; and (iii) long after the strong wave forcing that drives the SSWs has declined, diffusive fluxes of PV in equivalent latitude remain anomalously high in the lower stratosphere delaying the recovery of the vortex, with strong implications for the PV budget.

The acceleration of the residual circulation is characterized by enhanced polar downwelling and tropical upwelling throughout the whole depth of the stratosphere starting about 10 days before the central day of the SSW, with anomalies larger than 1.5 times the climatological standard deviation (σ) throughout the stratosphere at around lag −3 days (Figure 3). This anomalous stratospheric circulation changes sign right after the warming central date and can be explained by the cessation of wave forcing soon after that date. The weakened circulation lasts around 30 days in the upper stratosphere and up to 60 days in the lower stratosphere, both in the tropics and extratropics. Although it is generally accepted that the advective BDC is accelerated in winters with SSWs, the reversed and persistent anomalies after the SSW onset hinder a straightforward estimation of the seasonal anomalies of the BDC.

The anomalies in the mixing properties of the flow have a distinct signature (Figure 4). At 800 K ($\sim$10 hPa), enhanced mixing appears around 1 week before the central SSW day between 30° and 60°N in the surf zone. As the vortex shrinks and the PV gradients at the edge weaken the enhanced mixing migrates poleward, reaching its maximum (anomalies $> 1.8\sigma$) around 1–3 weeks after the SSW. After that, a band of poleward migrating reduced mixing dominates between 30° and 60°N. This behavior is increasingly delayed (and persistent) at lower altitudes: At 400 K ($\sim$100 hPa), the enhanced mixing appears about 1–2 weeks after the SSW centered at 60°N, barely moves in latitude, and disappears over 2 months later.

This composite overview is generally consistent with observational studies of trace gas evolution during individual SSWs. For example, Manney et al. (2009) combined calculations of the equivalent length derived from reanalysis fields and Aura Microwave Limb Sounder (MLS) data and found signatures of strong mixing in observations of polar CO during the 2006 SSW event; this enhanced mixing occurred over 3 weeks earlier in the upper than in the lower stratosphere. In a study of Arctic ozone loss during a split vortex event in the 2012/2013 winter, Manney, Lawrence, Santee, Livesey, et al. (2015) showed that mixing had a significant impact on observed trace species during the decay phase of the split event.

The large number of SSWs (152 events) identified in WACCM has allowed us to analyze, with statistical robustness, differences in zonal-mean transport and mixing between SSWs that occur during a PJO event (Kuroda & Kodera, 2001) from those SSWs that do not. Previous studies have shown that the former events (PJO-SSW) are characterized by a deeper penetration into the lower stratosphere of the wind and temperature anomalies during the onset of the warming event, a stronger and more rapid vortex recovery in the upper stratosphere, and an extended, slower recovery of the vortex in the lower stratosphere as compared to the latter events (nPJO-SSW) (e.g., Hitchcock, Shepherd & Manney, 2013). Our results indicate a clear distinction between PJO-SSW and nPJO-SSW in terms of transport and mixing, with the above-described evolution for all SSWs being intensified for PJO-SSWs, and the anomalies being generally weaker and less persistent for nPJO events. In the lower stratosphere at polar and tropical latitudes, the weakened residual circulation lasts over 90 days in the aftermath of PJO-SSW events, while it disappears after about 30 days from the central date of nPJO-SSW events (Figure 6). This distinction in the tropical upwelling for PJO events had not been noticed before and has potentially important impacts on tracer concentrations. The isentropic mixing anomalies are nearly twice as strong in the composite of PJO-SSW events at all levels analyzed, and in the lower stratosphere (350 and 400 K) any enhanced mixing for nPJO-SSW is barely statistically significant (Figure 7). Therefore, among all SSWs identified in WACCM, only those that are also PJO events have a strong, robust impact on the mixing properties of the flow in the lower stratosphere. Similar signals are seen in reanalysis composites, but the statistical significance is much weaker (not shown).

Because of the relevance of PV dynamics to understanding the stratospheric flow, we have further investigated the redistribution of PV on isentropic surfaces during and after SSWs. The change from geometrical coordinates to a tracer contour-based system (i.e., the equivalent latitude ϕ_e) necessary for the calculation of the equivalent length allows us to express the PV tendency as a function of the horizontal divergence of a diffusive flux F_d (Nakamura, 1996; Nakamura & Zhu, 2010) (this is not the only term governing the PV tendency, diabatic heating rates also play a role). A comparison between this diffusive PV flux F_d and the zonal-mean meridional eddy PV fluxes (i.e., $F_m = \bar{\sigma}_\theta \overline{\hat{v}\hat{P}}^*$) helps gain insights into processes controlling isentropic PV redistribution during SSWs. In the midstratosphere (800 K), the strong wave forcing that drives the SSW can be characterized by strong negative anomalies of eddy fluxes F_m that stop soon after the central day of the warming. The associated wave breaking elongates and stirs the PV field, which in turn enhances mixing (as characterized by positive Λ_{eq} anomalies, see Figures 7a and 7b) and diffuses PV out of the vortex (strong anomalies of F_d of opposite sign at each flank of the vortex edge, Figures 8a and 8b). After the central warming date, the F_m anomalies shut down, and positive anomalies of diffusive flux F_d contribute to the recovery of the vortex (compare Figures 8a, 8b, 10a, and 10b). In the lower stratosphere (400 K) there is clear distinction between PJO-SSW and nPJO-SSW, with practically no statistically significant anomalies in either the zonal-mean or the diffusive PV fluxes for nPJO-SSW events. In the case of PJO events, negative anomalies of F_d diffuse PV down gradient for up to 45 days after the SSW central day. These anomalies contribute to weakening the PV gradients at high latitudes and thus to delaying the recovery of the climatological conditions in the lower stratosphere. In contrast, from a zonal-mean perspective the eddy PV fluxes F_m are not statistically significant at 400 K (compare Figures 8 and 10).

These results indicate a complex relation between zonal-mean and equivalent latitude-based PV fluxes (i.e., the diffusive fluxes). Although enhanced mixing is associated with a well-stirred flow as a consequence of Rossby wave breaking, the temporal evolution of the zonal-mean eddy PV fluxes and the diffusive PV fluxes are manifestly not the same in the recovery period after SSWs, particularly for those that are also PJO events. It is suggested that these difference might be explained by diabatic effects and the decay of wave activity during this period (Haynes & McIntyre, 1987; Nakamura & Zhu, 2010). Abalos, Randel, et al. (2016) showed that the zonal-mean eddy PV fluxes provide valuable information on the spectral characteristics of stratospheric stirring and mixing in a climatological sense. Our results clearly demonstrate that in periods when the vortex undergoes dramatic changes in size and geometry (such as those during SSWs), the quasi-Lagrangian view of the PV evolution provided by the diffusive fluxes in equivalent latitude coordinates captures richer details of the PV redistribution (e.g., makes a clearer distinction of the interior of the vortex) than the zonal-mean eddy fluxes.

Acknowledgments

We are thankful to D. E. Kinnison and R. R. Garcia for performing the WACCM runs and providing the output, R. R. Garcia and W. J. Randel for insightful comments on an earlier version of this manuscript, and Gloria Manney and two anonymous reviewers for careful revisions that have helped improve the manuscript. A. de la Cámara has been supported by the Advanced Study Program at The National Center for Atmospheric Research (NCAR), which is sponsored by the U.S. National Science Foundation and by the Spanish project PALEOSTRAT (CGL2015-69699). M. Abalos has been supported by the NASA ACMAP program and by the research grant Atracción de Talento Comunidad de Madrid (ref: 2016-T2/AMB-1405), and Spanish project STEADY (CGL2017-83198-R). We would like to acknowledge high-performance computing support provided by NCAR's Computational and Information Systems Laboratory. Data from ERA-Interim are available at http://apps.ecmwf.int/datasets/; WACCM output is available at https://www2.acom.ucar.edu/gcm/ccmi-output and also upon request to the corresponding author.

References

Abalos, M., Legras, B., Ploeger, F., & Randel, W. J. (2015). Evaluating the advective Brewer-Dobson circulation in three reanalyses for the period 1979–2012. *Journal of Geophysical Research: Atmospheres*, *120*, 7534–7554. https://doi.org/10.1002/2015JD023182

Abalos, M., Legras, B., & Shuckburgh, E. (2016). Interannual variability in effective diffusivity in the upper troposphere/lower stratosphere from reanalysis data. *Quarterly Journal of the Royal Meteorological Society*, *142*(697), 1847–1861. https://doi.org/10.1002/qj.2779

Abalos, M., Randel, W. J., & Birner, T. (2016). Phase-speed spectra of eddy tracer fluxes linked to isentropic stirring and mixing in the upper troposphere and lower stratosphere. *Journal of the Atmospheric Sciences*, *73*(12), 4711–4730. https://doi.org/10.1175/JAS-D-16-0167.1

Baldwin, M. P., Gray, L. J., Dunkerton, T. J., Hamilton, K., Haynes, P. H., Randel, W. J., et al. (2001). The quasi-biennial oscillation. *Reviews of Geophysics*, *39*(2), 179–229. https://doi.org/10.1029/1999RG000073

Barnett, J. J., Corney, M., Murphy, A. K., Jones, R. L., Rodgers, C. D., Taylor, F. W., et al. (1975). Global and seasonal variability of the temperature and composition of the middle atmosphere. *Nature*, *313*, 505–530. https://doi.org/10.1038/313439a0

Butler, A. H., Seidel, D. J., Hardiman, S. C., Butchart, N., Birner, T., & Match, A. (2015). Defining sudden stratospheric warmings. *Bulletin of the American Meteorological Society*, *96*(11), 1913–1928. https://doi.org/10.1175/BAMS-D-13-00173.1

Charlton, A. J., & Polvani, L. M. (2007). A new look at stratospheric sudden warmings. Part I: Climatology and modeling benchmarks. *Journal of Climate*, *20*(3), 449–469. https://doi.org/10.1175/JCLI3996.1

Dee, D. P., Uppala, S. M., Simmons, A. J., Berrisford, P., Poli, P., Kobayashi, S., et al. (2011). The ERA-Interim reanalysis: Configuration and performance of the data assimilation system. *Quarterly Journal of the Royal Meteorological Society*, *137*(656), 553–597. https://doi.org/10.1002/qj.828

Dickinson, R. E. (1973). Method of parameterization for infrared cooling between altitudes of 30 and 70 kilometers. *Journal of Geophysical Research*, *78*(21), 4451–4457. https://doi.org/10.1029/JC078i021p04451

Dunkerton, T., Hsu, C-P. F., & McIntyre, M. E. (1981). Some Eulerian and Lagrangian diagnostics for a model stratospheric warming. *Journal of the Atmospheric Sciences*, *38*, 819–844. https://doi.org/10.1175/1520-0469(1981)038<0819:SEALDF>2.0.CO;2

Ebdon, R. A. (1960). Notes on the wind flow at 50 mb in tropical and subtropical regions in January 1957 and in 1958. *Quarterly Journal of the Royal Meteorological Society*, *86*, 540–542.

Fritz, S., & Soules, S. D. (1970). Large-scale temperature changes in the stratosphere observed from Nimbus 11. *Journal of the Atmospheric Sciences*, *27*(7), 1091–1097.

Fritz, S., & Soules, S. D. (1972). Planetary variations of stratospheric temperatures. *Monthly Weather Review*, *100*, 582–589. https://doi.org/10.1175/1520-0493(1972)100<0582:PVOST>2.3.CO;2

Garcia, R. R., Smith, A. K., Kinnison, D. E., de la Cámara, Á., & Murphy, D. J. (2017). Modification of the gravity wave parameterization in the Whole Atmosphere Community Climate Model: Motivation and results. *Journal of the Atmospheric Sciences*, *74*(1), 275–291. https://doi.org/10.1175/JAS-D-16-0104.1

Gómez-Escolar, M., Calvo, N., Barriopedro, D., & Fueglistaler, S. (2014). Tropical response to stratospheric sudden warmings and its modulation by the QBO. *Journal of Geophysical Research: Atmospheres*, *119*, 7382–7395. https://doi.org/10.1002/2013JD020560

Haynes, P., & Shuckburgh, E. (2000a). Effective diffusivity as a diagnostic of atmospheric transport: 1. Stratosphere. *Journal of Geophysical Research*, *105*(D18), 22,777–22,794. https://doi.org/10.1029/2000JD900093

Haynes, P., & Shuckburgh, E. (2000b). Effective diffusivity as a diagnostic of atmospheric transport: 2. Troposphere and lower stratosphere. *Journal of Geophysical Research*, *105*(D18), 22,795–22,810. https://doi.org/10.1029/2000JD900092

Haynes, P. H., & McIntyre, M. E. (1987). On the evolution of vorticity and potential vorticity in the presence of diabatic heating and frictional or other forces. *Journal of the Atmospheric Sciences*, *44*(5), 828–841.

Haynes, P. H., & McIntyre, M. E. (1990). On the conservation and impermeability theorems for potential vorticity. *Journal of the Atmospheric Sciences*, *47*(16), 2021–2031.

Haynes, P. H., McIntyre, M. E., Shepherd, T. G., Marks, C. J., & Shine, K. P. (1991). On the “Downward control” of the extratropical diabatic circulations by eddy-induced mean zonal forces. *Journal of the Atmospheric Sciences*, *48*(4), 651–678.

Hitchcock, P., & Shepherd, T. G. (2013). Zonal-mean dynamics of extended recoveries from stratospheric sudden warmings. *Journal of the Atmospheric Sciences*, *70*(2), 688–707. https://doi.org/10.1175/JAS-D-12-0111.1

Hitchcock, P., Shepherd, T. G., & Manney, G. L. (2013). Statistical characterization of Arctic polar-night jet oscillation events. *Journal of Climate*, *26*(6), 2096–2116. https://doi.org/10.1175/JCLI-D-12-00202.1

Hitchcock, P., Shepherd, T. G., Taguchi, M., Yoden, S., & Noguchi, S. (2013). Lower-stratospheric radiative damping and polar-night jet oscillation events. *Journal of the Atmospheric Sciences*, *70*(5), 1391–1408. https://doi.org/10.1175/JAS-D-12-0193.1

Kodera, K. (2006). Influence of stratospheric sudden warming on the equatorial troposphere. *Geophysical Research Letters*, *33*, L06804. https://doi.org/10.1029/2005GL024510

Kodera, K., Kuroda, Y., & Pawson, S. (2000). Stratospheric sudden warmings and slowly propagating zonal-mean zonal wind anomalies. *Journal of Geophysical Research*, *105*(D10), 12,351–12,359. https://doi.org/10.1029/2000JD900095

Kuroda, Y., & Kodera, K. (2004). Role of the Polar-night Jet Oscillation on the formation of the Arctic Oscillation in the Northern Hemisphere winter. *Journal of Geophysical Research*, *109*, D11112. https://doi.org/10.1029/2003JD004123

Kuroda, Y., & Kodera, K. (2001). Variability of the polar night jet in the Northern and Southern Hemispheres. *Journal of Geophysical Research*, *106*(D18), 20,703–20,713. https://doi.org/10.1029/2001JD900226

Lawrence, Z. D., & Manney, G. L. (2018). Characterizing stratospheric polar vortex variability with computer vision techniques. *Journal of Geophysical Research: Atmospheres*, *123*, 1510–1535. https://doi.org/10.1002/2017JD027556

Limpasuvan, V., Richter, J. H., Orsolini, Y. J., Stordal, F., & Kvissel, O. K. (2012). The roles of planetary and gravity waves during a major stratospheric sudden warming as characterized in WACCM. *Journal of Atmospheric and Solar-Terrestrial Physics*, *78-79*, 84–98. https://doi.org/10.1016/j.jastp.2011.03.004

Limpasuvan, V., Thompson, D. W., & Hartmann, D. L. (2004). The life cycle of the Northern Hemisphere sudden stratospheric warmings. *Journal of Climate*, *17*, 2584–2596.

Manney, G. L., & Lawrence, Z. D. (2016). The major stratospheric final warming in 2016: Dispersal of vortex air and termination of Arctic chemical ozone loss. *Atmospheric Chemistry and Physics*, *16*(23), 15,371–15,396. https://doi.org/10.5194/acp-16-15371-2016

Manney, G. L., Daffer, W. H., Strawbridge, K. B., Walker, K. A., Boone, C. D., Bernath, P. F., et al. (2008). The high Arctic in extreme winters: Vortex, temperature, and MLS and ACE-FTS trace gas evolution. *Atmospheric Chemistry and Physics*, *8*, 505–522. https://doi.org/10.5194/acpd-7-10235-2007

Manney, G. L., Harwood, R. S., MacKenzie, I. A., Minschwaner, K., Allen, D. R., Santee, M. L., et al. (2009). Satellite observations and modeling of transport in the upper troposphere through the lower mesosphere during the 2006 major stratospheric sudden warming. *Atmospheric Chemistry and Physics*, *9*(14), 4775–4795. https://doi.org/10.5194/acp-9-4775-2009

Manney, G. L., Lawrence, Z. D., Santee, M. L., Read, W. G., Livesey, N. J., Lambert, A., et al. (2015). A minor sudden stratospheric warming with a major impact: Transport and polar processing in the 2014/2015 Arctic winter. *Geophysical Research Letters*, *42*, 7808–7816. https://doi.org/10.1002/2015GL065864

Manney, G. L., Lawrence, Z. D., Santee, M. L., Livesey, N. J., Lambert, A., & Pitts, M. C. (2015). Polar processing in a split vortex: Arctic ozone loss in early winter 2012/2013. *Atmospheric Chemistry and Physics*, *15*(10), 5381–5403. https://doi.org/10.5194/acp-15-5381-2015

Marsh, D. R., Mills, M. J., Kinnison, D. E., Lamarque, J.-F., Calvo, N., & Polvani, L. M. (2013). Climate change from 1850 to 2005 simulated in CESM1(WACCM). *Journal of Climate*, *26*(19), 7372–7391. https://doi.org/10.1175/JCLI-D-12-00558.1

Matsuno, T. (1971). A dynamical model of the stratospheric sudden warming. *Journal of the Atmospheric Sciences*, *28*, 1479–1494. https://doi.org/10.1175/1520-0469(1971)028<1479:ADMOTS>2.0.CO;2

Müller, R., & Günther, G. (2003). A generalized form of Lait’s modified potential vorticity. *Journal of the Atmospheric Sciences*, *60*(17), 2229–2237. https://doi.org/10.1175/1520-0469(2003)060<2229:AGFOLM>2.0.CO;2

Nakamura, N. (1996). Two-dimensional mixing, edge formation, and permeability diagnosed in an area coordinate. *Journal of the Atmospheric Sciences*, *53*, 1524–1537. https://doi.org/10.1175/1520-0469(1996)053<1524:TDMEFA>2.0.CO;2

Nakamura, N., & Ma, J. (1997). Modified Lagrangian-mean diagnostics of the stratospheric polar vortices: 2. Nitrous oxide and seasonal barrier migration in the cryogenic limb array etalon spectrometer and SKYHI general circulation model. *Journal of Geophysical Research*, *102*(D22), 25,721–25,735. https://doi.org/10.1029/97JD02153

Nakamura, N., & Zhu, D. (2010). Finite-amplitude wave activity and diffusive flux of potential vorticity in eddy–mean flow interaction. *Journal of the Atmospheric Sciences*, *67*(9), 2701–2716. https://doi.org/10.1175/2010JAS3432.1

Plumb, R. A. (2002). Stratospheric transport. *Journal of the Meteorological Society of Japan*, *80*(4B), 793–809.

Randel, W. J., Garcia, R. R., & Wu, F. (2002). Time-dependent upwelling in the tropical lower stratosphere estimated from the zonal-mean momentum budget. *Journal of the Atmospheric Sciences*, *59*(13), 2141–2152. https://doi.org/10.1175/1520-0469(2002)059<2141:TDUITT>2.0.CO;2

Shuckburgh, E., Norton, W., Iwi, A., & Haynes, P. (2001). Influence of the quasi-biennial oscillation on isentropic transport and mixing in the tropics and subtropics. *Journal of Geophysical Research*, *106*(D13), 14,327–14,337. https://doi.org/10.1029/2000JD900664

Solomon, S., Kinnison, D., Bandoro, J., & Garcia, R. (2015). Simulation of polar ozone depletion: An update. *Journal of Geophysical Research: Atmospheres*, *120*, 7958–7974. https://doi.org/10.1002/2015JD023365

Tao, M., Konopka, P., Ploeger, F., Grooß, J.-U., Müller, R., Volk, C. M., et al. (2015). Impact of the 2009 major sudden stratospheric warming on the composition of the stratosphere. *Atmospheric Chemistry and Physics*, *15*(15), 8695–8715. https://doi.org/10.5194/acp-15-8695-2015